Supporting Information for

Tailoring Carrier Dynamics in Perovskite Solar Cells via Precise Dimension and Architecture Control and Interfacial Positioning of Plasmonic Nanoparticles

Xun Cui,[a,b] Yihuang Chen,[a] Meng Zhang,[a] Yeu Wei Harn,[a] Jiabin Qi,[a] Likun Gao,[a] Zhong Lin Wang,[a] Jinsong Huang,[c] Yingkui Yang,[b,*] and Zhiqun Lin[a,*]

[a] School of Materials Science and Engineering, Georgia Institute of Technology, Atlanta, GA 30332, USA
[b] Key Laboratory of Catalysis and Energy Materials Chemistry of Ministry of Education & Hubei Key Laboratory of Catalysis and Materials Science, South-Central University for Nationalities, Wuhan 430074, China
[c] Department of Applied Physical Sciences, University of North Carolina, Chapel Hill, NC 27599, USA

The Supporting Information file includes:

1. Experimental Section

2. Figure S1-S17

Figure S13. Nyquist plots of electrochemical impedance spectroscopy (EIS) for perovskite $CH_3NH_3PbI_3$ solar cells (a) with and (b) without Au NPs sandwiched within a double-layer TiO_2 ETL under 1 sun illumination at various applied bias from 0 to 0.8 V. (c) The equivalent circuit for fitting the impedance spectroscopy. (d) Recombination resistance derived from both (a) and (b) as a function of applied bias of devices with and without Au NPs embedded between a double-layer TiO_2 ETL.

Figure S14. Schematic illustration of the device configuration. (a) FTO/Au NPs-sandwiched double-layer TiO_2/Ag, and (b) FTO/a double-layer TiO_2/Ag.

Figure S15. Mott-Schottky plots of planar perovskite $CH_3NH_3PbI_3$ solar cells with and without Au NPs embedded within a double-layer TiO_2 ETL.

Figure S16. The statistic distribution of (a) short-circuit current density J_{sc}, (b) open-circuit voltage V_{oc}, and (c) fill factor *FF* for 30 mesostructured perovskite $FA_{0.85}MA_{0.15}PbI_{2.55}Br_{0.45}$ solar cells with and without Au NPs embedded between a double-layer TiO_2 ETL.

Figure S17. The stability of (a) planar perovskite $FA_{0.85}MA_{0.15}PbI_{2.55}Br_{0.45}$ solar cells and (b) mesostructured perovskite $FA_{0.85}MA_{0.15}PbI_{2.55}Br_{0.45}$ solar cells without encapsulation yet stored in the desiccator and evaluated under ambient condition (temperature: 25 ± 2 °C, relative humidity: 30 ± 5%).

3. Table S1-S5

Table S1. Summary of molecular weights of amphiphilic star-like PAA-*b*-PS diblock copolymer and P4VP-*b*-P*t*BA-*b*-PEO triblock copolymers and the corresponding dimensions of plain Au and Au/SiO_2 core/shell nanoparticles.

Table S2. Summary of the Au core dimeter and the SiO_2 shell thickness for plain Au and Au/SiO_2 core/shell nanoparticles in Figure 1.

Table S3. Summary of the photovoltaic parameters of perovskite $CH_3NH_3PbI_3$ solar cells fabricated using different layers of TiO_2.

Table S4. Summary of the photovoltaic parameters of perovskite solar cells fabricated with pristine TiO_2 as well as with plain Au NPs and Au/SiO_2 core/shell NPs placed at the TiO_2 ETL/perovskite $CH_3NH_3PbI_3$ interface (scenario 2).

Table S5. Summary of the photovoltaic parameters of perovskite $CH_3NH_3PbI_3$ solar cells fabricated with pristine TiO_2 as well as with plain Au NPs and Au/SiO_2 core/shell NPs sandwiched within two layers of TiO_2 ETL (scenario 1).

4. Note S1-S2

Note S1: Optimization of the TiO_2 ETL thickness.

Note S2: Device performance based on the assembly scenario 2.

1. Experimental Section

1.1 Materials

Methylammonium iodide (CH_3NH_3I; MAI), formamidinium iodide (H_2NCHNH_2I; FAI) and methylammonium bromide (CH_3NH_3Br; MABr) were synthesized according to the reported method[1, 2], and dried in a vacuum oven at 50 °C for 24 h. Gold(III) chloride trihydrate ($HAuCl_4 \cdot 3H_2O$, ≥99.9%), TFA (99%), titanium diisopropoxide bis(acetylacetonate) (Tiacac, 75 wt% in isopropanol), titanium(IV) chloride ($TiCl_4$, 99.995%), lead iodide (PbI_2, 99.999%), lead bromide ($PbBr_2$, 99.999%), dimethylformamide (DMF, anhydrous, 99.8%), tetraethoxysilane (TEOS, 99.999%), 2-Bromoisobutyryl bromide (98%), tris[2-(dimethylamino)ethyl] amine (Me6-TREN, 97%), *N,N,N′,N″,N″*-pentamethyldiethylene triamine (PMDETA, 99%), anhydrous 1-methyl-2-pyrrolidinone (NMP, 99.5%), trifluoroacetic acid (TFA, 99.9%), propargyl bromide solution (80 wt% in toluene), diphenyl ether (DPE, 99%), and isopropanol (IPA, anhydrous, 99.5%) were purchased from Sigma-Aldrich and used as received. CuBr (98%, Sigma-Aldrich) and CuCl (98%, Sigma-Aldrich) were purified via stirring overnight in acetic acid, filtered, washed with ethanol and diethyl ether completely, and dried under vacuum. *β*-Cyclodextrin (*β*-CD, Sigma-Aldrich) and poly(ethylene oxide) methyl ether (mPEO, M_n = 5000) were used as received. Alkyne-terminated mPEO was prepared according to the literature (*26*). *tert*-Butyl acrylate (*t*BA, Sigma-Aldrich 98%), anisole (TCI America, 99.0%), methyl ethyl ketone (Fisher Scientific, ≥99.9%) and N,N-dimethylformamide (DMF, Fisher Scientific, ≥99.9%) were distilled over CaH_2 under reduced pressure prior to use. Tetrahydrofuran (THF, 99%) was stirring over potassium wire and distilled from potassium naphthalenide solution. 4-Vinylpyridine (4VP, Sigma-Aldrich 95%) was distilled over CaH_2 under reduced pressure prior to use. Diphenylmethyl sodium (DPMNa) (c = 0.52 M) was synthesized according to the literature.[3] Styrene (St, Sigma-Aldrich, ≥99%) was washed with 10% NaOH aqueous solution and water successively, dried over anhydrous $MgSO_4$ and CaH_2 sequentially, and distilled under reduced pressure. All other reagents were purified by common purification procedures.

1.2 Synthesis of Star-Like PAA-*b*-PS Diblock Copolymer

Heptakis[2,3,6-tri-*O*-(2-bromo-2-methylpropionyl)]-*β*-cyclodextrin (denoted 21Br-*β*-CD) was synthesized according to our previous work.[4] Using 21Br-*β*-CD as the macroinitiator, star-like P*t*BA-*b*-PS diblock copolymer was prepared by sequential ATRP of *t*BA, St monomers. Briefly, for the first ATRP, CuBr (52.5 mg), PMDETA (127.5 mg), 21Br-*β*-CD (75 mg) and *t*BA (31.5 mL) in MEK (1 mL *t*BA in 1 mL solvent) were placed in an argon purged ampule, followed by three freeze-pump-thaw degassing cycles. After reacting at 60 ^{o}C for a desired time, the product was collected and purified by fractional precipitation using methanol/water (1/1 in volume) as precipitator, yielding star-like P*t*BA-Br. The second ATRP reaction started with mixture of styrene : star-like P*t*BA-Br (i.e., Br in P*t*BA macroinitiator) : CuBr : PMDETA = 800 : 1 : 1 : 2 (molar ratio) in anisole (1 g St in 1 mL solvent) in an argon purged ampule, followed by three freeze-pump-thaw degassing cycles. The reaction was performed at 90 ^{o}C and purified through the same procedure above, yielding star-like P*t*BA-*b*-PS. Star-like P*t*BA-*b*-PS was further hydrolyzed in $CHCl_3$ (50 mL, 10 mg/mL) in the presence of 4 mL TFA, resulting in star-like PAA-*b*-PS.

1.3 Synthesis of Star-Like P4VP-*b*-P*t*BA-*b*-PEO Triblock Copolymer

Using 21Br-*β*-CD-based macroinitiator, star-like P4VP-*b*-P*t*BA-*b*-PEO triblock copolymer was prepared by sequential ATRP of 4VP, *t*BA monomers, followed by a click reaction. For the first ATRP, CuCl (36.2 mg), Me6-TREN (170.3 mg), 21Br-*β*-CD (75 mg) and 4VP (30 mL) in 2-propanol (1 mL 4VP in 1 mL solvent) were mixed in an argon purged ampule, followed by three freeze-pump-thaw degassing cycles. After reacting at 40 ^{o}C for a desired time, the product was collected and purified by precipitation using chloroform and hexane, yielding star-like P4VP-Cl. The second ATRP reaction was performed using mixture of *t*BA : star-like P4VP-Cl (i.e., Cl in P4VP macroinitiator) : CuCl : Me6-TREN = 800 : 1 : 1 : 2 (molar ratio) in methyl ethyl ketone (1 g *t*BA in 1 mL solvent) in an argon purged ampule, followed by three freeze-pump-thaw degassing cycles. The reaction was performed at 60 ^{o}C and precipitated with an excess of cold methanol, yielding star-like P4VP-*b*-P*t*BA-Cl. Star-like P4VP-*b*-P*t*BA-Cl was end-functionalized with azide groups (i.e., star-like P4VP-*b*-P*t*BA-N_3)

using sodium azide (Cl in star-like P4VP-*b*-P*t*BA-Cl : sodium azide = 1 : 10; molar ratio) in DMF (0.3 g/mL). For click reaction, mixture of PEO-alkyne : -N_3 in starlike P4VP-*b*-P*t*BA-N_3 : copper bromide : Me6-TREN = 1.5 : 1 : 10 : 10; molar ratio) was degassed and reacted at 90 ^oC for 24 h. The product was precipitated in cold methanol and dried under vacuum, yielding star-like P4VP-*b*-P*t*BA-*b*-PEO.

1.4 Synthesis of Plain Au NPs

For synthesis of plain Au NPs, amphiphilic PAA-*b*-PS diblock copolymers were used as nanoreactors to template the nucleation and growth of monodisperse plasmonic Au NPs capped with PS blocks that are originally covalently connected to the inner PAA blocks. In a typical procedure, PAA-*b*-PS diblock copolymer template (10 mg) was dissolved in the mixed solvents of DMF/benzyl alcohol (DMF : BA = 9 : 1 by volume), followed by the addition of $HAuCl_4 \bullet 3H_2O$ as precursor with TBAB as reducer. The precursors were preferably incorporated within the regime occupied by PAA blocks. The mixture was stirred for 1 h under argon at room temperature to ensure that all the chemicals to be completely dissolved and then immersed in an oil bath at 60 °C under argon for 2 h. The mixture was then purified by ultracentrifugation with toluene as solvent and ethanol as precipitant several times to remove the remaining precursors and mixed solvents, yielding Au NPs intimately and stably capped with PS (i.e., PS-capped Au NPs).

1.5 Synthesis of Au/SiO_2 core/shell NPs

For comparison, Au/SiO_2 core/shell NPs were synthesized using star-like P4VP-*b*-P*t*BA-*b*-PEO as nanoreactors. In a typical process, 10 mg star-like P4VP-*b*-P*t*BA-*b*-PEO was dissolved in a mixture of dimethylformamide (DMF) and diphenyl ether (DPE) at DMF : DPE = 9 : 1 in volume at room temperature. An appropriate amount of $HAuCl_4$ (with TBAB as the reducer) were added and incorporated into the compartment containing inner star-like P4VP blocks via the strong interaction between pyridal groups of P4VP blocks in star-like P4VP-*b*-P*t*BA-*b*-PEO and the metal moieties of Au precursors ($HAuCl_4$). The reaction was performed at 60 °C under argon for 2 h, yielding Au core nanoparticles intimately capped by P*t*BA-*b*-PEO

blocks. The intermediate P*t*BA blocks were then hydrolyzed in the presence of TFA into poly(acrylic acid) (PAA), which was used as template for SiO_2 shell. Typically, a certain amount of SiO_2 precursor, TEOS (0.5 mL), and ammonia (0.3 mL) were added to the reaction solution. Similarly, in the mixed solvents of DMF : DPE = 9 : 1 (by volume), the interaction between the carboxyl groups of PAA blocks and the precursor TEOS produced the SiO_2 shell. The thickness of the SiO_2 shell can be precisely tuned by varying the molecular weight of the intermediate P*t*BA blocks (**Table S1**).

1.6 Device Fabrication

FTO glass substrates (surface resistivity: ~7 Ω/sq) were patterned by etching with 6 M HCl and zinc powder, and then thoroughly cleaned with detergent, water, isopropanol, acetone, and ethanol in sequence in an ultrasonic bath for 30 min. FTO glass was then oxygen plasma-treated for 15 min prior to use. To prepare the compact TiO_2 (c-TiO_2) layer, the 0.15 M Tiacac solution was spin-coated on the cleaned FTO substrates at 1000 rpm for 10 s and 4000 rpm for 30 s and then annealed at 150 °C for 30 min. After cooling down, plasmonic NPs solution (i.e., the PS-capped Au NPs toluene solution or the PEO-capped Au/SiO_2 core/shell NPs ethanol solution) was spin-coated on the first TiO_2 layer, yielding a monolayer thick nanoparticles coated on the first TiO_2 surface. Subsequently, a second TiO_2 layer was then spun onto the as-obtained film to encapsulate the plasmonic NPs (i.e., scenario 1 for positioning as-synthesized plasmonic NPs). After annealing at 150 °C for 30 min and sintering treatment at 450 °C for 30 min (during which PS and PEO ligands situated on the surface of Au NPs and Au/ Au/SiO_2 were effectively removed), the substrates were transferred into glovebox. For scenario 2 used to position as-synthesized plasmonic NPs, the plasmonic NPs solution was spin-coated on twice-deposited TiO_2 layer as in scenario 1 yet without plasmonic NPs (i.e., placing a monolayer-thick plasmonic NPs at the perovskite/TiO_2 interface) with the same experimental condition as noted in scenario 1. The abovementioned devices are for preparing planar PSCs. On the other hand, to fabricate mesostructured devices, the TiO_2 paste was spin-coated on the compact TiO_2-coated FTO glass substrate at 4000 rpm for 30 s, followed by sintering treatment at 500 °C for 30 min to yield mesoporous TiO_2 layer. For devices prepared using $CH_3NH_3PbI_3$,

the $CH_3NH_3PbI_3$ layer was one-step deposited. The precursor solution of $CH_3NH_3PbI_3$ was prepared by stirring 461 mg of PbI_2, 159 mg of CH_3NH_3I, and 78 mg of DMSO in 600 mg of DMF solution at room temperature for 3 h. The completely dissolved solution was spun on the as-obtained TiO_2-Au NPs-TiO_2 film (i.e., scenario 1) at 4000 rpm for 25 s. After 8 s of spin-coating, 0.5 ml of diethyl ether was quickly dripped onto the center of the spinning substrate. After annealing for 20 min on a 100 °C hotplate, the as-prepared films turned from colorless to dark brown, indicative of the formation of $CH_3NH_3PbI_3$. Similarly, the optimized $FA_{0.85}MA_{0.15}PbI_{2.55}Br_{0.45}$ perovskite layer was produced by spin-coating. The perovskite precursor solution was prepared by dissolving FAI, MABr, PbI_2 and $PbBr_2$ at a molar ratio of FAI : MABr : PbI_2 : $PbBr_2$ = 0.85 : 0.15 : 2.55 : 0.45 in DMSO. The solution concentration was 1.2 M. The precursor solution was maintained at 90 °C. It was then spin-coated on a FTO substrate at 4000 rpm for 25 s, followed by thermal annealing at 150 °C for 20 min to form the perovskite film. Subsequently, the spiro-MeOTAD solution was spin-coated on the perovskite layer at 2000 rpm for 30 s. The spiro-MeOTAD solution was prepared by dissolving 0.08 g spiro-MeOTAD in 1 ml chlorobenzene, in which 30 μl 4-tertbutyl pyridine and 20 μl lithium bis(trifluoromethanesulfonyl)imide (Li-TFSI) solution (500 mg Li-TSFI in 1 ml acetonitrile) were added. Finally, a 120-nm silver layer was deposited on the spiro-MeOTAD layer by thermal evaporation at a constant evaporation rate of 0.1 nm/s under a vacuum of 2×10^{-6} mbar.

1.7 Characterization

The molecular weight of star-like block copolymer nanoreactors was measured by an Agilent-1100 gel permeation chromatography (GPC) equipped with a G1362A refractive detector and a G1314A variable wavelength detector, in which one 5 μm LP gel column (500 Å, molecular range: 500 ~ 2×104 g/mol) and two 5 μm LP gel mixed bed columns (molecular range: 200 ~ 3×106 g/mol) were calibrated with PS standard samples. The morphologies of plasmonic NPs were imaged using a JEOL 100CX transmission electron microscopy (TEM). The morphologies of $CH_3NH_3PbI_3$ and TiO_2 films and devices were characterized using a LEO 1550 scanning electron microscopy (SEM). The plasmonic properties of Au NPs and perovskite films were measured by UV-vis spectroscopy (Varian; UV-vis-NIR

spectrophotometer, Cary 5000). The steady-state photoluminescence was collected using spectrofluorophotometer (RF-5301PC, SHIMADZU). The time-resolved photoluminescence measurements were performed using a Photon Technology International (PTI) LaserStrobe Spectrofluorometer equipped with a PTI GL-3300 nanosecond nitrogen laser (λ=337 nm) and Photomultiplier tubes (PMT) together with time-correlated single photon counting (TCSPC) for single collection and analysis. Perovskite solar cells were tested under AM1.5G irradiation using a Newport LCS-100 Solar Simulator (100 $mWcm^{-2}$, calibrated with a Newport 91150V Reference Cell System). The current density-voltage (*J-V*) curves were obtained using a Keithley 2400 multisource meter. A shadow mask was used to fix the measuring area of devices. The incident photon to charge carrier efficiency (IPCE) was measured using a Newport Quantum Efficiency/IPCE Measurement Kit. The conductivity measurement was performed using a Zennium PP211 Electrochemical Workstation. The electrochemical impedance spectra (EIS) analysis was performed at various biases (V= 0-0.8 V) under simulated 100 mW cm^{-2} AM 1.5G illumination with the frequency ranging from 1 MHz to 1 Hz and amplitude (mV) = 5. The Mott-Schottky analysis through capacitance-voltage measurements was collected by Zennium PP211 Electrochemical Workstation at 10 kHz with the bias potentials ranging from 0 to 1.2 V. A small AC voltage of 50 mV was used for probing the actual capacitance at a given bias. The built-in potentials of the devices were obtained from Mott-Schottky plots. The intensity modulated photocurrent/photovoltage spectroscopy (IMPS/IMVS) measurements were recorded on a Zennium PP211 Electrochemical Workstation, together with light source control module. The IMPS/IMVS measurements were conducted using a blue LED light (wavelength of 450 nm) with the tuned light frequency from 1 KHz to 5 MHz. In IMPS and IMVS measurements, the photocurrent and photovoltage response are used to evaluate charge transit time (τ_d by IMPS) and carrier lifetime (τ_n by IMVS) in perovskite solar cells by the equation $\tau_d = 1/(2\pi f_d)$, and $\tau_n = 1/(2\pi f_n)$, where f_d and f_n are the frequencies of the minima of the IMPS and IMVS imaginary component, respectively.[5-7] Accordingly, the carriers diffusion coefficient D_n can be obtained from $D_n = d^2/(2.35\ \tau_d)$, where *d* is the thickness of the TiO_2 photoanode.[8] The work function changes after illumination were investigated by a kelvin probe force microscopy (KPFM).

2. Figure S1-S17

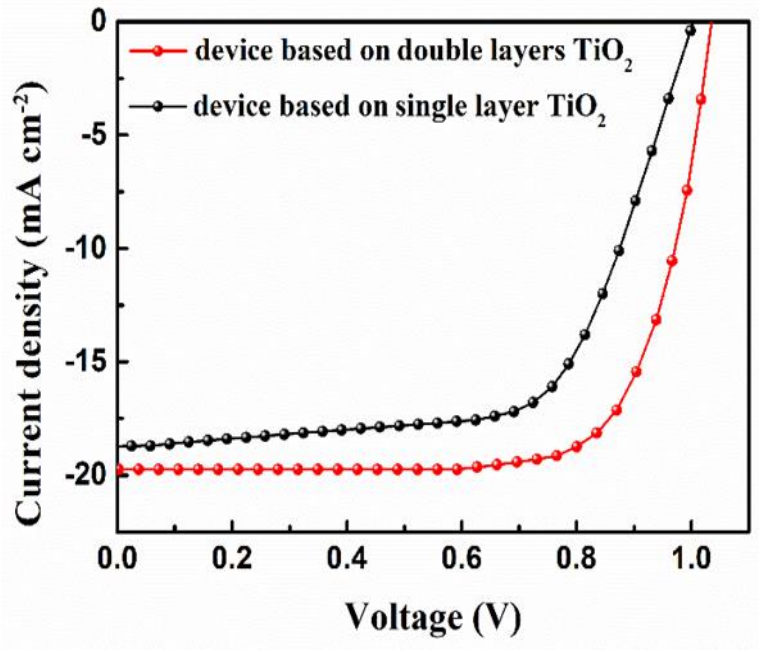

Figure S1. *J-V* curves for perovskite solar cells fabricated with different layers of TiO_2.

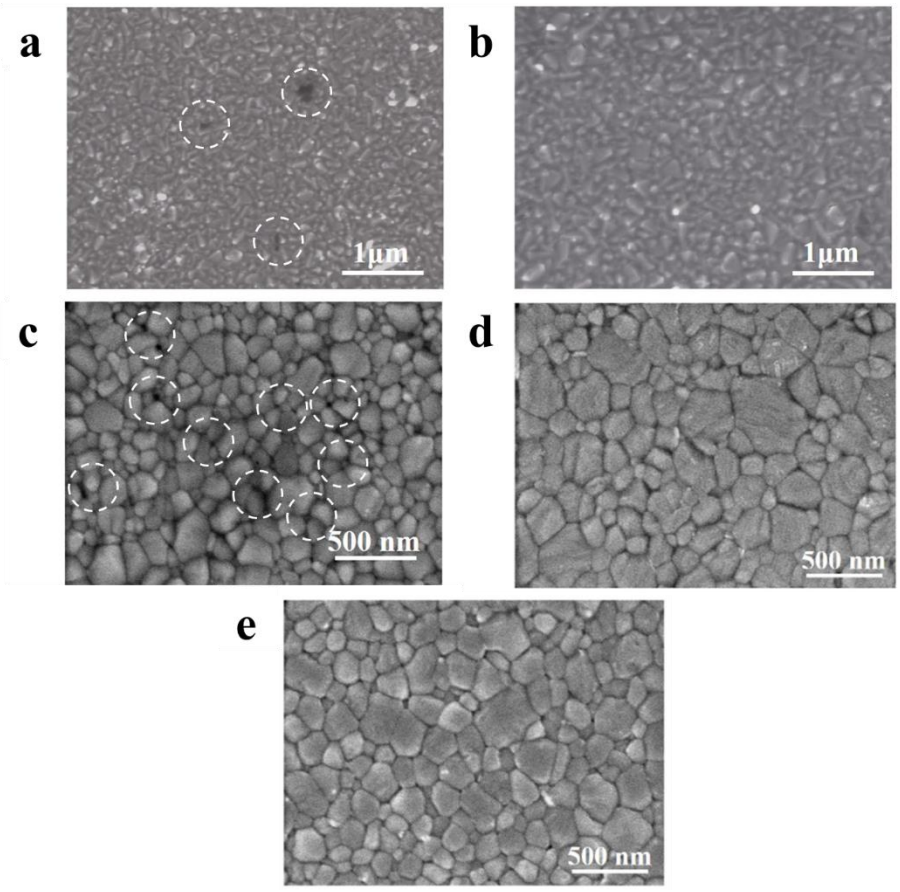

Figure S2. SEM images of (a) a single-layer TiO_2 film and (b) a double-layer TiO_2 film, as well as the perovskite film deposited on (c) a single-layer TiO_2 film, (d) a double-layer TiO_2 film, and (e) a double-layer TiO_2 film with Au NPs sandwiched.

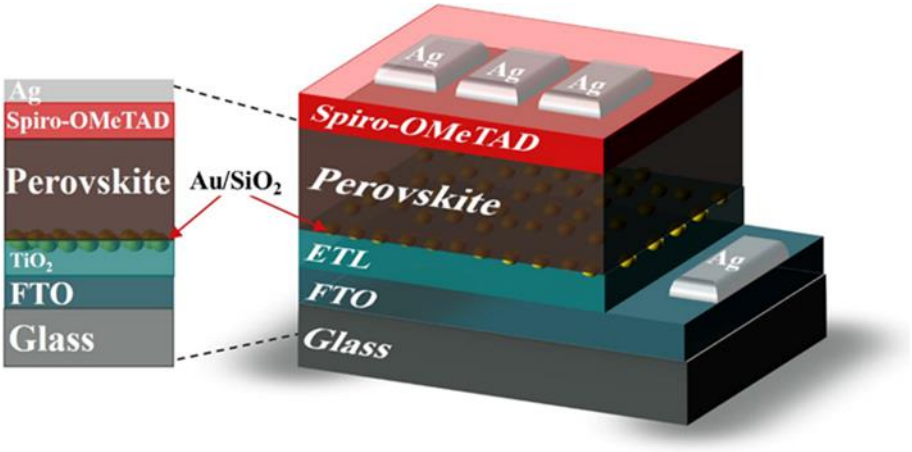

Figure S3. Schematic of the perovskite solar cells assembled by placing plasmonic NPs (plain Au or Au/SiO_2 core/shell) at the TiO_2 ETL/perovskite $CH_3NH_3PbI_3$ interface.

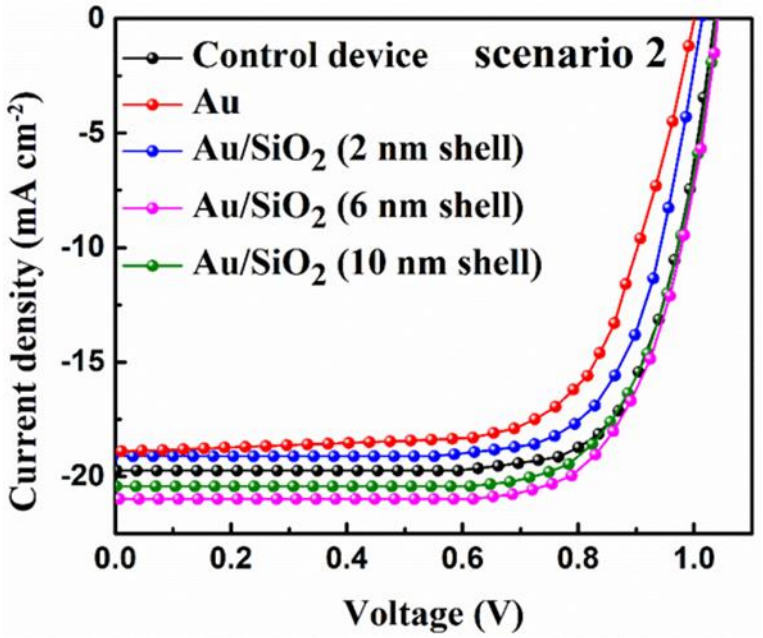

Figure S4. *J-V* characteristics of devices fabricated with pristine TiO_2 (control device; no plasmonic NPs), with Au NPs and Au/SiO_2 NPs of different SiO_2 shell thickness at the TiO_2/perovskite $CH_3NH_3PbI_3$ interface.

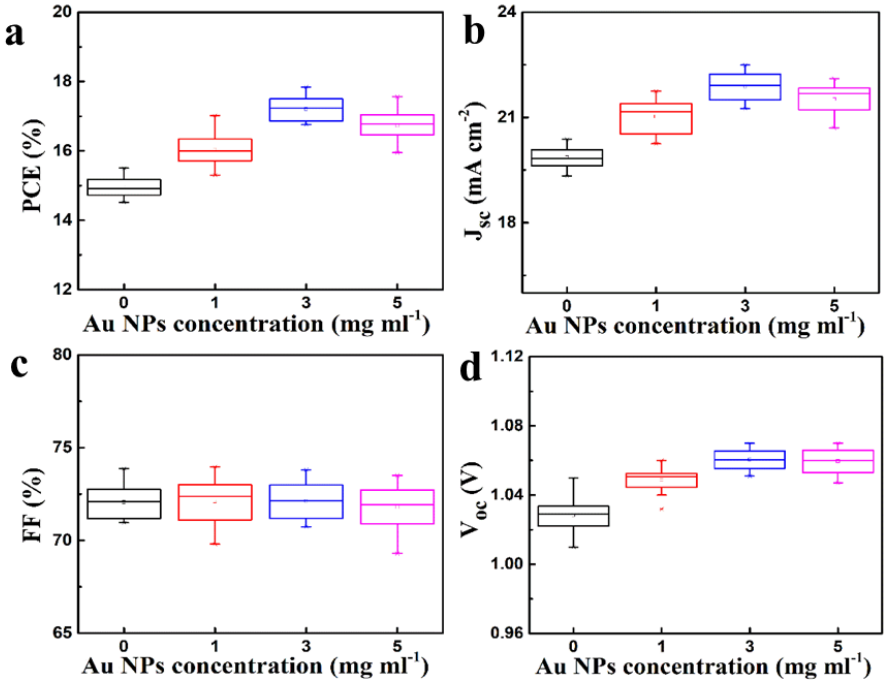

Figure S5. Statistical analysis of characteristics of perovskite $CH_3NH_3PbI_3$ solar cells by varying the concentration of Au NPs solution. (a) Power conversion efficiency *PCE*, (b) short-circuit current density J_{sc}, (c) fill factor *FF*, and (d) open-circuit voltage V_{oc}.

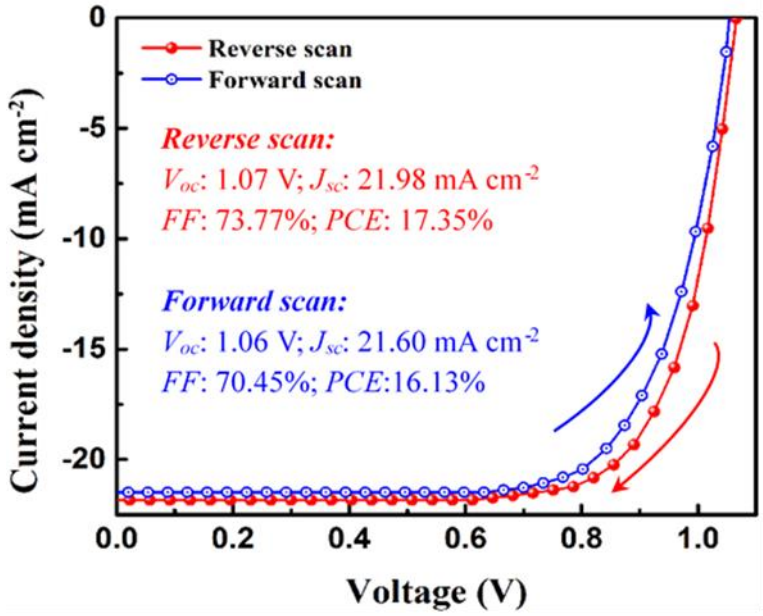

Figure S6. *J-V* characteristics for the perovskite $CH_3NH_3PbI_3$ solar cell with plain Au NPs embedded between a double-layer TiO_2 ETL.

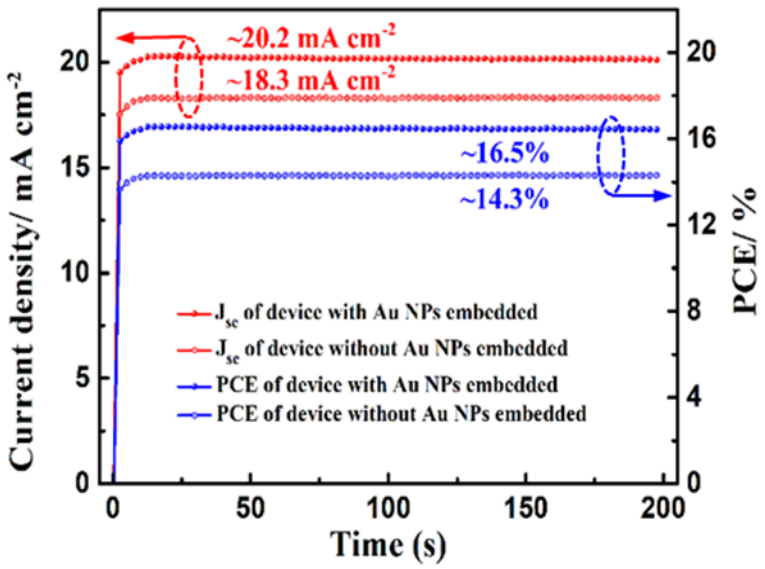

Figure S7. Steady-state *PCE* and photocurrent density of perovskite $CH_3NH_3PbI_3$ solar cells with and without (i.e., control device) plain Au NPs embedded between a double-layer TiO_2 ETL.

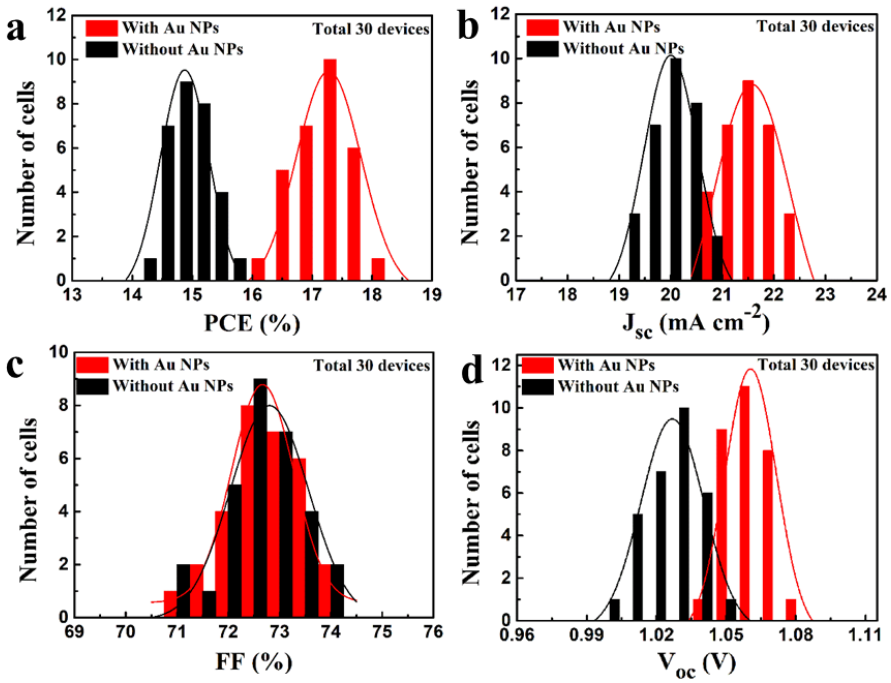

Figure S8. The statistic distribution of (a) short-circuit current density J_{sc}, (b) open-circuit voltage V_{oc}, (c) fill factor *FF*, and (d) power conversion efficiency *PCE* of 30 planar perovskite $CH_3NH_3PbI_3$ solar cells with and without Au NPs embedded between a double-layer TiO_2 ETL.

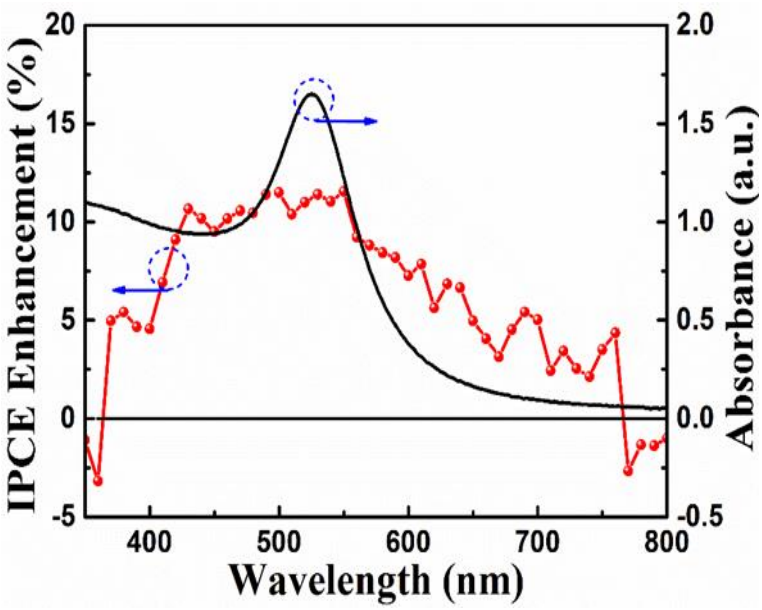

Figure S9. IPCE enhancement (i.e., the difference of IPCE for PSCs with and without sandwiching Au NPs in a double-layer TiO_2; $IPCE_{with\ Au\ NPs} - IPCE_{without\ Au\ NPs}$) after embedding Au NPs in the planar perovskite $CH_3NH_3PbI_3$ solar cell. UV-vis spectrum of Au NPs in solution.

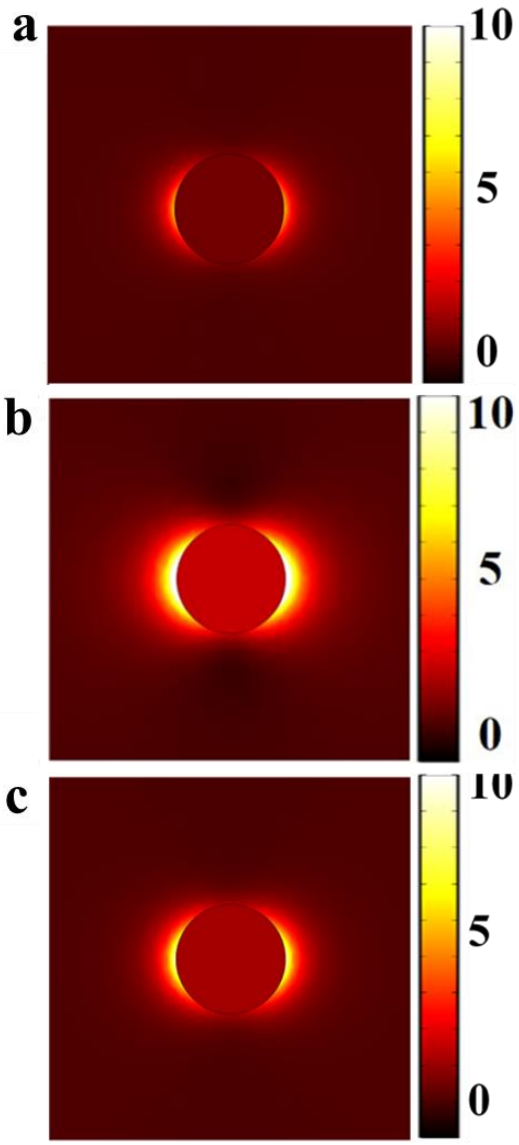

Figure S10. Simulated electric field profile for incident light with a wavelength of (a) 500 nm, (b) 525 nm, and (c) 575 nm.

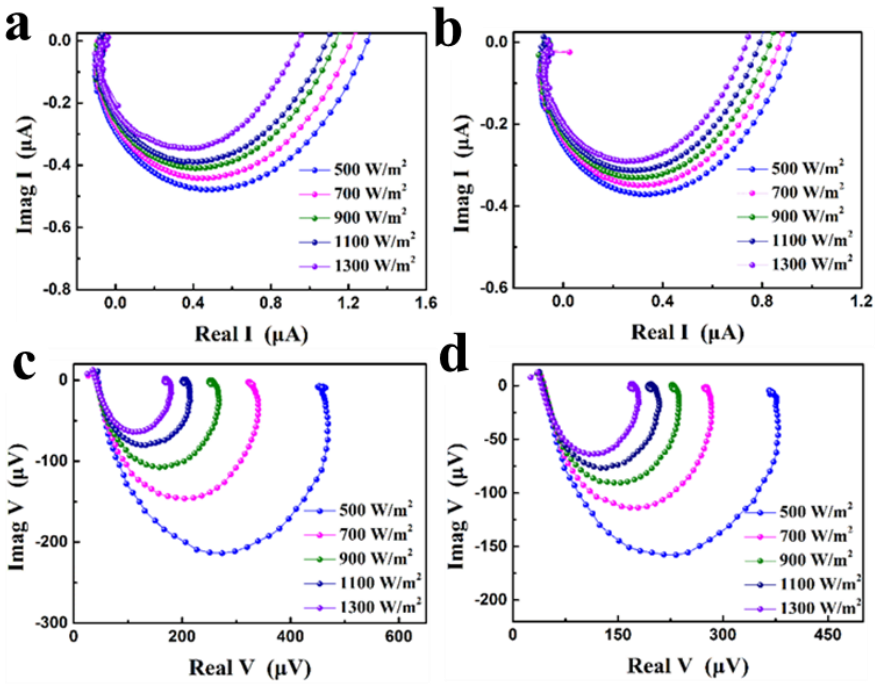

Figure S11. (a, b) IMPS and (c, d) IMVS plots of perovskite $CH_3NH_3PbI_3$ solar cells based on a double-layer TiO_2 ETL (a, c) with and (b, d) without Au NPs sandwiched.

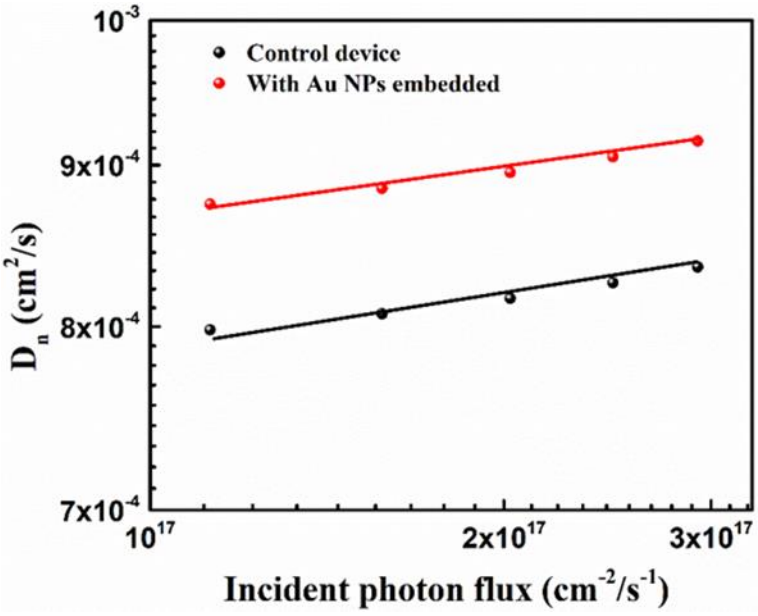

Figure S12. Carrier diffusion coefficients (D_n) for perovskite $CH_3NH_3PbI_3$ solar cells with and without Au NPs incorporated between a double-layer of TiO_2.

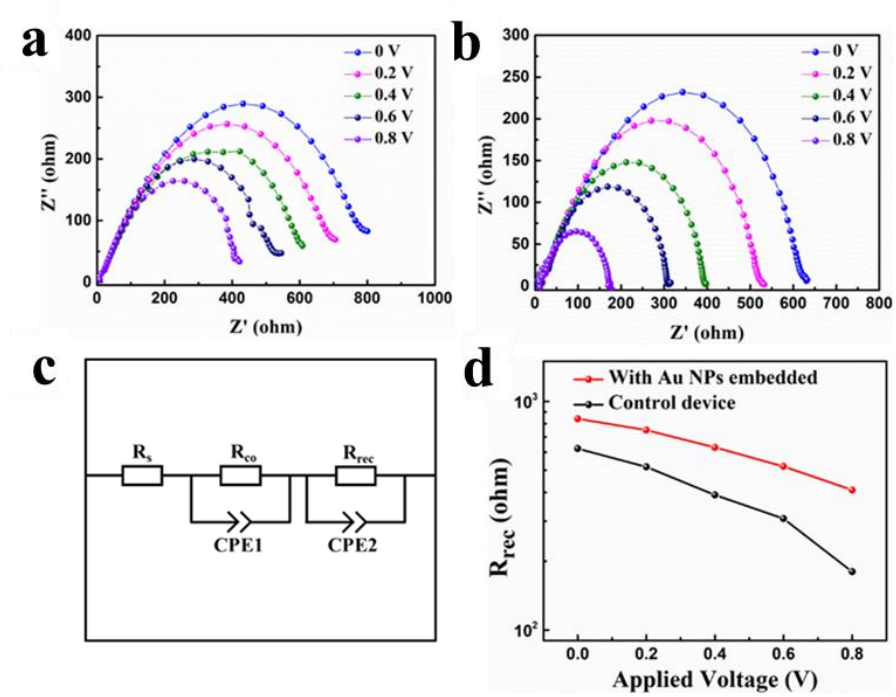

Figure S13. Nyquist plots of electrochemical impedance spectroscopy (EIS) for perovskite $CH_3NH_3PbI_3$ solar cells (a) with and (b) without Au NPs sandwiched within a double-layer TiO_2 ETL under 1 sun illumination at various applied bias from 0 to 0.8 V. (c) The equivalent circuit for fitting the impedance spectroscopy. (d) Recombination resistance derived from both (a) and (b) as a function of applied bias of devices with and without Au NPs embedded between a double-layer TiO_2 ETL.

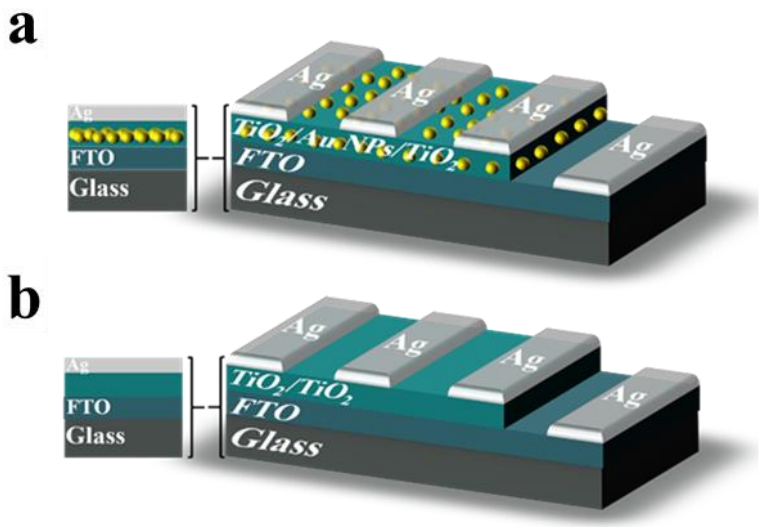

Figure S14. Schematic illustration of the device configuration. (a) FTO/Au NPs-sandwiched double-layer TiO_2/Ag, and (b) FTO/a double-layer TiO_2/Ag.

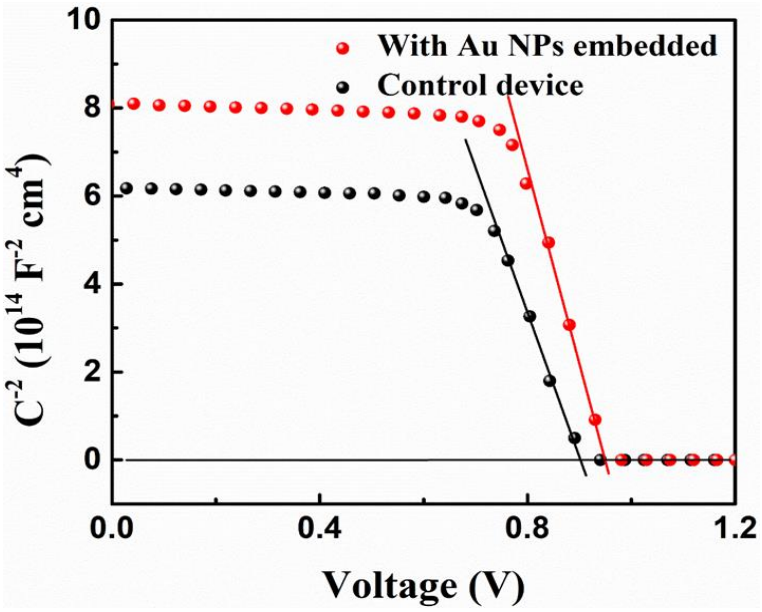

Figure S15. Mott-Schottky plots of planar perovskite $CH_3NH_3PbI_3$ solar cells with and without Au NPs embedded within a double-layer TiO_2 ETL.

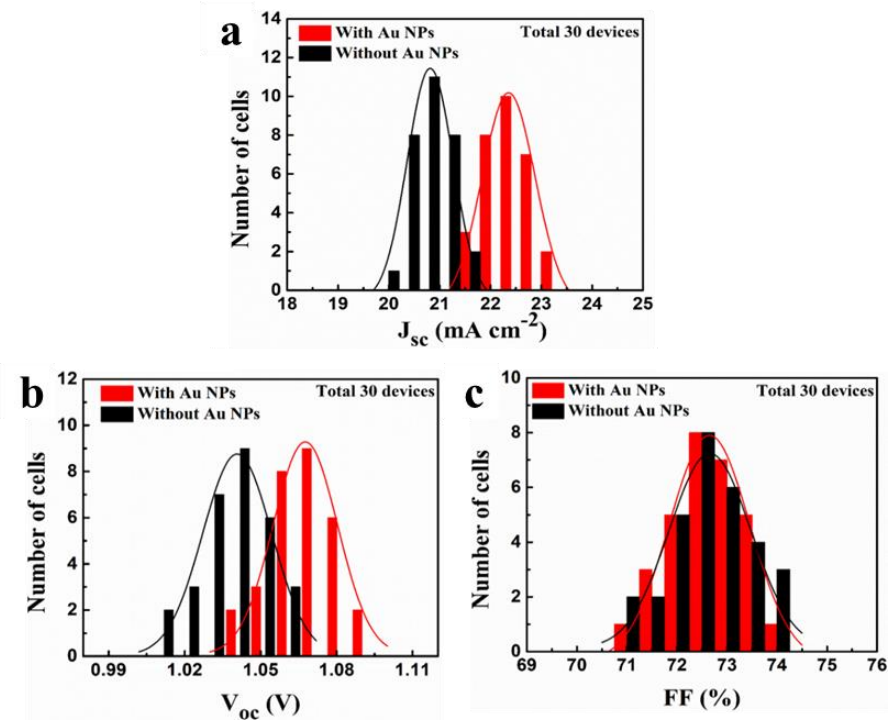

Figure S16. The statistic distribution of (a) short-circuit current density J_{sc}, (b) open-circuit voltage V_{oc}, and (c) fill factor *FF* for 30 mesostructured perovskite $FA_{0.85}MA_{0.15}PbI_{2.55}Br_{0.45}$ solar cells with and without Au NPs embedded between a double-layer TiO_2 ETL.

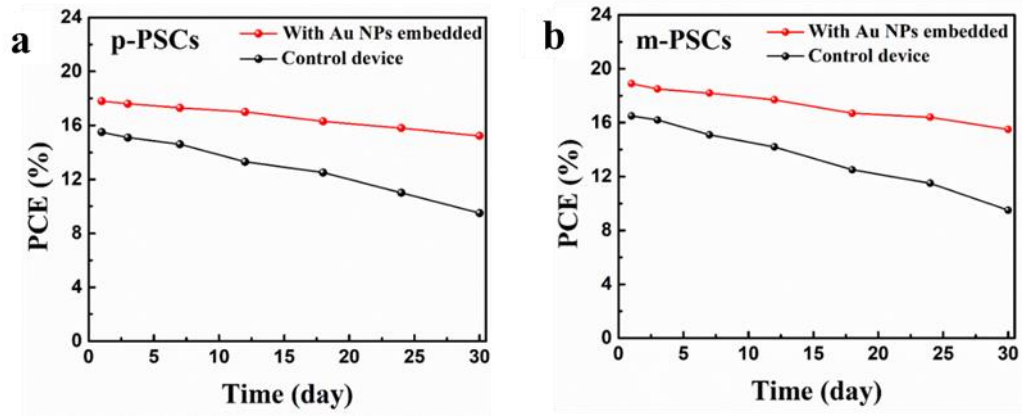

Figure S17. The stability of (a) planar perovskite $FA_{0.85}MA_{0.15}PbI_{2.55}Br_{0.45}$ solar cells and (b) mesostructured perovskite $FA_{0.85}MA_{0.15}PbI_{2.55}Br_{0.45}$ solar cells without encapsulation yet stored in the desiccator and evaluated under ambient condition (temperature: 25 ± 2 °C, relative humidity: 30 ± 5%).

3. Table S1-S5

Table S1. Summary of molecular weights of amphiphilic star-like PAA-*b*-PS diblock copolymer and P4VP-*b*-P*t*BA-*b*-PEO triblock copolymers and the corresponding dimensions of plain Au and Au/SiO_2 core/shell nanoparticles.

Dimensions of nanoparticles	$M_{n,\ P4VP}$	$M_{n,\ PtBA}$	$M_{n,\ PEO}$	$M_{n,\ PAA}$	$M_{n,\ PS}$	***PDI***
Au (12 nm)	/	/	/	11,200	5100	1.12
Au/SiO_2 (12 nm/2 nm)	11,800	3500	5000	/	/	1.14
Au/SiO_2 (12 nm/6 nm)	11,800	12,400	5000	/	/	1.15
Au/SiO_2 (12 nm/10 nm)	11,800	22,900	5000	/	/	1.17
M_n **of each arm was calculated from ^{1}H-NMR data. The polydispersity index,** ***PDI*** **was determined by GPC.**						

Table S2. Summary of the Au core dimeter and the SiO_2 shell thickness for plain Au and Au/SiO_2 core/shell nanoparticles in **Figure 1**.

Nanoparticles	**Au core diameter**	**SiO_2 shell thickness**
Au (12 nm)	12.1 ± 0.5	/
Au/SiO_2 (12 nm/2 nm)	11.9 ± 0.4	1.8 ± 0.3
Au/SiO_2 (12 nm/6 nm)	12.2 ± 0.3	6.3 ± 0.4
Au/SiO_2 (12 nm/10 nm)	12.0 ± 0.5	10.2 ± 0.5

Table S3. Summary of the photovoltaic parameters of perovskite $CH_3NH_3PbI_3$ solar cells fabricated using different layers of TiO_2.

Device based on different layers of TiO_2	***V_{oc}* (V)**	***J_{sc}* (mA cm^{-2})**	***FF* (%)**	***PCE* (%)**
Single-layer TiO_2	1.00±0.02	18.71±0.72	65.15±1.92	12.19±0.71
Double-layer TiO_2	1.03±0.02	19.85±0.53	72.41±1.46	15.01±0.49

Table S4. Summary of the photovoltaic parameters of perovskite solar cells fabricated with pristine TiO_2 as well as with plain Au NPs and Au/SiO_2 core/shell NPs placed at the TiO_2 ETL/perovskite $CH_3NH_3PbI_3$ interface (*scenario 2*).

Devices	***V_{oc}* (V)**	***J_{sc}* (mA cm^{-2})**	***FF* (%)**	***PCE* (%)**
Control device	1.03±0.02	19.85±0.53	72.41±1.46	15.01±0.49
Plain Au NPs	0.99±0.03	18.91±0.75	68.91±1.05	12.90±0.46
Au/SiO_2 NPs (2 nm SiO_2)	1.01±0.02	19.11±0.68	70.35±1.16	14.06±0.62
Au/SiO_2 NPs (6 nm SiO_2)	1.03±0.02	20.98±0.50	72.12±1.26	15.80±0.41
Au/SiO_2 NPs (10 nm SiO_2)	1.02±0.02	20.43±0.49	71.87±1.65	15.33±0.53

Table S5. Summary of the photovoltaic parameters of perovskite $CH_3NH_3PbI_3$ solar cells fabricated with pristine TiO_2 as well as with plain Au NPs and Au/SiO_2 core/shell NPs sandwiched within two layers of TiO_2 ETL (*scenario 1*).

Devices	V_{oc} **(V)**	J_{sc} **(mAcm^{-2})**	***FF*** **(%)**	***PCE*** **(%)**
Control device	1.03±0.02	19.85±0.53	72.41±1.46	15.01±0.49
Plain Au NPs	1.06±0.01	21.87±0.62	72.27±1.53	17.30±0.54
Au/SiO_2 NPs (2 nm SiO_2)	1.05±0.02	21.19±0.55	72.39±0.97	16.58±0.36
Au/SiO_2 NPs (6 nm SiO_2)	1.02±0.01	20.81±0.77	72.48±1.03	15.87±0.47
Au/SiO_2 NPs (10 nm SiO_2)	1.02±0.02	20.44±0.49	72.02±1.11	15.31±0.43

4. Note S1-S2

Note S1: Optimization of the TiO_2 ETL thickness

We note that unless otherwise specified, all the tables (**Tables S3-S5**) and figures (**Figures S4-S9, S11-13, and S15**) in Supporting Information are obtained based on the devices assembled using $CH_3NH_3PbI_3$ as the perovskite absorber.

It is notable that the charge transport properties and the uniform film coverage of the whole TiO_2 ETL should be balanced. We found that the device based on a single-layer TiO_2 only yields an average PCE of **12.19**%, which is inferior compared to the one using a double-layer TiO_2 prepared by spin-coating a second TiO_2 layer on the first TiO_2 layer (average PCE = **15.01**%). Further increasing TiO_2 ETL thickness leads to deteriorate perovskite device performance due to the increased serial resistance. Current density versus voltage (*J-V*) curves of these two kind devices are plotted in **Figure S1**, and detailed parameters statistics are summarized in **Table S3**. The device based on single-layer TiO_2 degrades dramatically during the *J-V* test, which may result from poor coverage of TiO_2 ETL on the FTO substrate and poor quality of perovskite film on the TiO_2 ETL. On the one hand, the TiO_2 ETL/perovskite interface plays an important role in charge collection within PSCs, where a pinhole free and uniform TiO_2 ETL is desired for effective charge extraction. The top view SEM image of as-obtained single-layer TiO_2 (**Figure S2a**) shows a poor film coverage (marked with white circles) compared with that of double-layer TiO_2 (**Figure S2b**). The poor TiO_2 ETL coverage can result in serious recombination of the induced electrons and holes. Moreover, the quality of perovskite film can also significantly influence the performance of PSCs, where a pinhole-free perovskite film with large crystalline grain is favorable for effective charge carrier separation and transport. SEM images of perovskite films deposited on single-layer TiO_2 and double-layer TiO_2 are presented in **Figure S2c** and **S2d**, respectively. For perovskite film deposited on single-layer TiO_2, more pin holes (marked with white circles) are observed on the surface after annealing process. These pin holes may lead to a direct contact between HTL and TiO_2 ETL, and thus a high possibility of short circuit condition. The film quality of perovskite is improved when deposited on a double-layer TiO_2, revealing that a thicker layer of TiO_2 favors perovskite

growth. This observation correlates well with the prior results that a thicker TiO_2 ETL achieves a better perovskite film quality under the same condition.[9,10] However, an overly thick TiO_2 ETL leads to an increased serial resistance and thus impedes the charge carrier collection. Taken together, a double-layer TiO_2 film is optimized to yield an optimum device performance.

Note S2: Device performance based on the assembly scenario 2

Typical current density-voltage (*J-V*) characteristics of device fabricated using pristine TiO_2 with plain Au NPs incorporated at the TiO_2 ETL/perovskite $CH_3NH_3PbI_3$ interface are plotted in **Figure S4** and the detailed parameters statistics are summarized in **Table S4**. Notably, device fabricated with plain Au NPs deposited at the TiO_2 ETL/perovskite interface exhibits a poor fill factor (*FF*), a weak short-circuit current density (J_{sc}), and a low open-circuit voltage (V_{oc}) simultaneously, yielding an inferior average PCE of **12.90**%. This device performance is even poorer than that of control device (average PCE: **15.01**%). We then introduced separately the Au/SiO_2 core/shell NPs with a shell thickness of 2 nm, 6 nm, and 10 nm at the TiO_2 ETL/perovskite interface. Similarly, device based on Au/SiO_2 NPs with a shell thickness of 2 nm placed at the TiO_2 ETL/perovskite interface also displays a relatively inferior performance (average PCE: **14.06**%). Quite interestingly, when increasing the thickness of dielectric SiO_2 shell capped on the Au core to 6 nm, the device shows an enhanced J_{sc} with nearly unchanged V_{oc} and *FF* compared to control device and thus a superior average PCE of **15.80**%. Further increased thickness of the dielectric SiO_2 shell (10 nm) results in a slightly decreased performance (**Figure S4**). Clearly, the prevention of direct contact between Au NPs and the perovskite absorber by capping a protective SiO_2 layer with a suitable thickness can effectively minimize the carrier recombination on the Au surface, so an enhanced PCE of the corresponding device can be achieved. A scrutiny of the *J-V* curves (**Figure S4**) and parameters statistics (**Table S4**) of devices based on Au/SiO_2 core/shell NPs with a shell thickness of 6 nm and 10 nm, we found that the enhanced PCEs are largely determined by J_{sc} yet V_{oc} and *FF*. For plasmon-mediated perovskite absorber, it has been reported that the plasmonic near electromagnetic field (NEF) impacts greatly and effectively around the LSPR wavelength and when the active material is located in extremely close proximity to the metallic NPs.[11] As the

SiO_2 shell thickness of Au/SiO_2 NPs increases, the active perovskite $CH_3NH_3PbI_3$ is distanced further from the Au core and thus experiences a less NEF enhancement accompanied by a decrease in J_{sc} (**Figure S4**). Thus, the improved plasmonic effect in Au/SiO_2 NPs with a SiO_2 shell thickness of 6 nm compared to that with 10 nm is likely due to the more optimal NEF in collaboration with the active perovskite and the TiO_2 ETL. As a result, devices based on Au/SiO_2 NPs with a SiO_2 shell thickness of 6 nm exhibit the best performance (average PCE: **15.80**%) in scenario 2. The improved J_{sc} is indicative of a facilitated carrier separation and transfer at the TiO_2 ETL/perovskite $CH_3NH_3PbI_3$ interface with plasmonic Au/SiO_2 NPs. Recent research has already credited the performance improvement to the LSPR-induced enhancement of light absorption and promotion of carrier transport and collection in this typical structure where metallic NPs are embedded near the active layer.[12]

Supplementary References

1. G. E. Eperon, S. D. Stranks, C. Menelaou, M. B. Johnston, L. M. Herz and H. J. Snaith, *Energy Environ. Sci.*, 2014, **7**, 982-988.
2. J. H. Heo, S. H. Im, J. H. Noh, T. N. Mandal, C.-S. Lim, J. A. Chang, Y. H. Lee, H.-j. Kim, A. Sarkar and M. K. Nazeeruddin, *Nat. Photonics*, 2013, **7**, 486.
3. Z. Li, P. Li and J. Huang, *J. Polym. Sci., Part A: Polym. Chem.*, 2006, **44**, 4361-4371.
4. X. Pang, L. Zhao, M. Akinc, J. K. Kim and Z. Lin, *Macromolecules*, 2011, **44**, 3746-3752.
5. J. Wang, I. Mora-Seró, Z. Pan, K. Zhao, H. Zhang, Y. Feng, G. Yang, X. Zhong and J. Bisquert, *J. Am. Chem. Soc.* 2013, **135**, 15913-15922.
6. J. H. Heo, H. J. Han, D. Kim, T. K. Ahn and S. H. Im, *Energy Environ. Sci.*, 2015, **8**, 1602-1608.
7. J. H. Heo, D. H. Song, H. J. Han, S. Y. Kim, J. H. Kim, D. Kim, H. W. Shin, T. K. Ahn, C. Wolf, T.-W. Lee and S. H. Im, *Adv. Mater.*, 2015, **27**, 3424-3430.
8. B. Wang, M. Zhang, X. Cui, Z. Wang, M. Rager, Y. Yang, Z. Zou, Z. L. Wang and Z. Lin, *Angew. Chem. Int. Ed.*, 2019, **58**, 2-10.
9. Z. Yuan, Z. Wu, S. Bai, Z. Xia, W. Xu, T. Song, H. Wu, L. Xu, J. Si and Y. Jin, *Adv. Energy Mater.*, 2015, **5**.
10. G. E. Eperon, V. M. Burlakov, P. Docampo, A. Goriely and H. J. Snaith, *Adv. Funct. Mater.*, 2014, **24**, 151-157.
11. J.-H. Im, I.-H. Jang, N. Pellet, M. Grätzel and N.-G. Park, *Nat. Nanotechnol.*, 2014, **9**, 927-932.
12. K. Chan, M. Wright, N. Elumalai, A. Uddin and S. Pillai, *Adv. Opt. Mater.*, 2017, **5**.